

A comparison of nonlinear mixing models for vegetated areas using simulated and real hyperspectral data

Nicolas Dobigeon⁽¹⁾, Laurent Tits⁽²⁾, Ben Somers⁽³⁾,
Yoann Altmann⁽¹⁾ and Pol Coppin⁽²⁾

⁽¹⁾ University of Toulouse, IRIT/INP-ENSEEIH/TéSA, Toulouse, France

{Nicolas.Dobigeon,Yoann.Altmann}@enseeiht.fr

⁽²⁾ Department of Biosystems, Katholieke Universiteit Leuven, 3001 Leuven, Belgium

{Laurent.Tits,Pol.Coppin}@biw.kuleuven.be

⁽³⁾ Division Forest, Nature and Landscape, Katholieke Universiteit Leuven, 3001 Leuven, Belgium

ben.somers@ees.kuleuven.be

Abstract

Spectral unmixing is a crucial processing step when analyzing hyperspectral data. In such analysis, most of the work in the literature relies on the widely acknowledged linear mixing model to describe the observed pixels. Unfortunately, this model has been shown to be of limited interest for specific scenes, in particular when acquired over vegetated areas. Consequently, in the past few years, several nonlinear mixing models have been introduced to take nonlinear effects into account. These models have been proposed empirically, however without any thorough validation. In this paper, the authors take advantage of two sets of real and physical-based simulated data to validate the accuracy of various nonlinear models in vegetated areas. These physics-based and analysis models, and their corresponding unmixing algorithms, are evaluated with respect to their ability of fitting the measured spectra and of providing an accurate estimation of the abundance coefficients, considered as the spatial distribution of the materials in each pixel.

Index Terms

Hyperspectral imagery, spectral unmixing, nonlinear spectral mixtures, vegetated areas, ray tracing.

I. INTRODUCTION

Spectral unmixing (SU) of hyperspectral images consists of extracting the spectral responses $\mathbf{m}_1, \dots, \mathbf{m}_R$ of the R macroscopic materials (or *endmembers*) present in the imaged scene and, for each pixel \mathbf{y}_p of the image ($p = 1, \dots, P$), estimating the corresponding proportions $a_{1,p}, \dots, a_{R,p}$ (or *abundances*) that represent the spatial distributions of these materials over the area of interest [1]. The first automated unmixing techniques have been proposed in the early 1990's [2]. When no prior knowledge is available regarding the studied scene, SU can be usually decomposed into two successive steps. First, the endmembers are extracted from the image and, subsequently, the proportions of the materials are estimated in a so-called *inversion* step. A vast majority of the endmember extraction algorithms (EEA) and inversion techniques exploit some geometrical concepts that are intrinsically related to an assumption of a linear mixing process to explain the observed pixels. In other words, under this linear mixing model (LMM), each observed pixel of a given image is assumed to result from the linear combination of the R endmember spectra

$$\mathbf{y}_p^{(\text{LMM})} = \sum_{r=1}^R a_{r,p} \mathbf{m}_r + \mathbf{n}_p = \mathbf{M} \mathbf{a}_p + \mathbf{n}_p \quad (1)$$

where $\mathbf{a}_p = [a_{1,p}, \dots, a_{R,p}]^T$ denotes the proportions of the R material in the p th pixel, $\mathbf{M} = [\mathbf{m}_1, \dots, \mathbf{m}_R]$ is the endmember matrix and \mathbf{n}_p stands for an additive residual term accounting for the measurement noise and modeling error. Since the mixing coefficients $a_{1,p}, \dots, a_{R,p}$ are expected to represent the actual spatial distribution of the materials in the p th pixel, they are commonly subject to the following positivity and sum-to-one (or additivity) constraints

$$\begin{cases} a_{r,p} \geq 0, & \forall r, \forall p \\ \sum_{r=1}^R a_{r,p} = 1, & \forall p. \end{cases} \quad (2)$$

This LMM has received a considerable attention in the image processing and remote sensing literature since it represents an acceptable first-order approximation of the physical processes involved in most of the scenes of interest [2]. Consequently, it has motivated a lot of research works that aim at developing efficient endmember extraction algorithms (EEA), designed to recover pure spectral signatures in the image, and inversion techniques to estimate the abundance coefficients for a given (estimated or *a priori* known) set of endmembers. Comprehensive overviews of these EEA and inversion methods can be found in [1]–[3]. Specifically, two main approaches have been advocated to solve the inversion step, that can be formulated as a constrained optimization problem solved by fully constrained least

square algorithms [4]–[6] or as a statistical estimation problem solved within a Bayesian framework [7]–[9].

However, for specific applications, LMM has demonstrated some difficulties to accurately describe real mixtures [10]. In particular, scenes acquired over vegetated areas are known to be subjected to more complex interactions that can not be properly taken into account by a simple LMM [11]–[13]. Indeed, for these specific scenarios of interest, differences in evaluation between the transparent 3D vegetation canopies and the relatively flat soil surfaces submit photons to multipath and scattering effects. Therefore, various attempts have been conducted to overcome the intrinsic limitations of the LMM. A large family of nonlinear models that have been proposed to analyzed vegetated areas can be described as

$$\mathbf{y}_p = \mathbf{M}\mathbf{a}_p + \boldsymbol{\mu}(\mathbf{M}, \mathbf{a}_p, \mathbf{b}_p) + \mathbf{n}_p. \quad (3)$$

In (3), the observed pixel is composed of a linear contribution similar to the LMM and an additive nonlinear term $\boldsymbol{\mu}(\cdot)$ that may depend on the endmember matrix \mathbf{M} , the abundance coefficients in \mathbf{a}_p and additional nonlinearity coefficients \mathbf{b}_p introduced to adjust the amount of nonlinearity in the pixel. This class of models includes the bilinear models [14], the quadratic-linear model [15], the post-nonlinear model [16] and the bilinear-bilinear model [17] (the most commonly used will be fully described in Section II).

However, to our knowledge, all these models have been motivated in various research works based on empirical and intuitive considerations, without any careful and throughout analysis of their ability to properly describe real mixtures. In this article, we propose to fill this gap by evaluating the relevance of various nonlinear models. Specifically, requirements for ensuring the quality of a model are twofold: i) this model should be sufficiently flexible to fit the real observations in various external conditions and ii) it should be able to account for the relative spatial distribution of the materials in the pixel, with the prime objective to estimate the abundance coefficients. To meet this challenge, we take advantage of an interesting set of simulated and in-situ collected hyperspectral data. First, we use a detailed virtual orchard and forest model constructed in a physically based ray-tracing environment using detailed sub-models for the description of tree geometry, leaf and soil bidirectional reflectance and diffuse illumination [18]–[20]. The model has thoroughly been validated with field observations [18] and more recently we could provide, based on a comparison with in-situ data, strong evidence that our ray tracing model realistically describes the spectral scattering and thus nonlinearity observed in vegetated areas [13]. Second, we use data from an in-situ experiment in a commercial citrus orchard. This experiment comprised in-situ measured mixed pixel reflectance spectra, pixel specific endmember spectra and subpixel cover fraction distributions. This unique dataset of in-situ measured mixed pixel reflectance spectra has previously been used to study nonlinearity in fruit orchards [12].

The paper is organized as follows. Section II introduces the main nonlinear models that have been proposed in the literature to describe mixtures encountered in vegetated areas are described. The ray-tracer based simulated data and the in-situ measurements used to validate these models are described in Section III. The experiment results obtained by using the previously introduced nonlinear models on the two sets of data are reported in Section IV. A comprehensive discussion on these results is conducted in Section V. Section VI concludes the paper.

II. NONLINEAR MIXING MODELS

A. Bilinear models

To take into account the scattering effects the photons are subjected to before reaching the sensor, a wide class of nonlinear models are derived by defining the nonlinear component $\mu(\mathbf{M}, \mathbf{a}_p, \mathbf{b}_p)$ in (3) as a sum of bilinear terms [14]

$$\mu(\mathbf{M}, \mathbf{a}_p, \mathbf{b}_p) \triangleq \sum_{i=1}^{R-1} \sum_{j=i+1}^R b_{i,j,p} \mathbf{m}_i \odot \mathbf{m}_j$$

where the operator \odot stands for a termwise product

$$\mathbf{m}_i \odot \mathbf{m}_j \triangleq \begin{pmatrix} m_{1,i} m_{1,j} \\ \vdots \\ m_{L,i} m_{L,j} \end{pmatrix}. \quad (4)$$

The set of nonlinearity coefficients $\{b_{i,j,p}\}_{i,j}$ allows the amount of nonlinearity in the p th pixel to be adjusted between each pair of materials \mathbf{m}_i and \mathbf{m}_j . The various bilinear models of the literature mainly differ by the definition of these coefficients $b_{i,j,p}$ and the associated constraints they are subject to. The most common models, that will be evaluated in Section IV, are recalled below.

In [12] and [21], the authors propose to include the nonlinearity coefficients $\{b_{i,j,p}\}_{i,j}$ within the set of constraints (2) defined by the LMM, leading to

$$\mathbf{y}_p^{(\text{NM})} \triangleq \sum_{r=1}^R a_{r,p} \mathbf{m}_r + \sum_{i=1}^{R-1} \sum_{j=i+1}^R b_{i,j,p} \mathbf{m}_i \odot \mathbf{m}_j + \mathbf{n}_p \quad (5)$$

with

$$\begin{cases} a_{r,p} \geq 0, & \forall r, \forall p \\ b_{i,j,p} \geq 0, & \forall r, \forall i \neq j \\ \sum_{r=1}^R a_{r,p} + \sum_{i=1}^{R-1} \sum_{j=i+1}^R b_{i,j,p} = 1, & \forall p. \end{cases} \quad (6)$$

Note that this model, denoted NM for Nascimento's model in this article, reduces to the LMM when $b_{i,j,p} = 0, \forall i \neq j$. This is an interesting property since the LMM is known to be an admissible first approximation of the actually involved physical processes. However, in that case, the abundance coefficients $\{a_{r,p}\}_{r=1}^R$ are not subject to the sum-to-one constraints defined in (2).

In [22], Fan *et al.* have defined the nonlinearity coefficients $b_{i,j,p}$ as the product of the abundances, $b_{i,j,p} \triangleq a_{i,p}a_{j,p}$, under the LMM-based constraints in (2), leading to the so-called Fan's Model (FM)

$$\mathbf{y}_p^{(\text{FM})} \triangleq \sum_{r=1}^R a_{r,p} \mathbf{m}_r + \sum_{i=1}^{R-1} \sum_{j=i+1}^R a_{i,p} a_{j,p} \mathbf{m}_i \odot \mathbf{m}_j + \mathbf{n}_p. \quad (7)$$

The main motivation for relating the amount of nonlinear interactions (governed by $b_{i,j,p}$) to the amount of linear contribution (governed by $a_{i,p}$ and $a_{j,p}$) is straightforward: the more a given material is present in the pixel, the more nonlinear interactions may occur. In particular, if a component \mathbf{m}_i is absent in the p th pixel, then $a_{i,p} = 0$ and consequently $b_{i,j,p} = 0$, which means that there are no interactions between the material \mathbf{m}_i and any other materials \mathbf{m}_j ($j \neq i$). Note however that this bilinear model does not extend the LMM.

To cope with this later limitation, the generalized bilinear model (GBM) [23] weights the products of abundances $a_{i,p}a_{j,p}$ by additional free parameters $\gamma_{i,j,p} \in (0, 1)$ that tune the amount of nonlinear interactions, leading to $b_{i,j,p} \triangleq \gamma_{i,j,p}a_{i,p}a_{j,p}$ and

$$\mathbf{y}_p^{(\text{GBM})} \triangleq \sum_{r=1}^R a_{r,p} \mathbf{m}_r + \sum_{i=1}^{R-1} \sum_{j=i+1}^R \gamma_{i,j,p} a_{i,p} a_{j,p} \mathbf{m}_i \odot \mathbf{m}_j + \mathbf{n}_p. \quad (8)$$

The GBM has the nice properties of i) generalizing the LMM by enforcing $\gamma_{i,j,p} = 0$ ($\forall i, j$), similarly to NM but contrary to FM and ii) having the amount of nonlinear interactions to be proportional to the material abundances, similarly to FM but contrary to NM.

B. Post-nonlinear mixing model

Inspired by pioneered works in blind source separation [24], Altmann *et al.* have introduced in [16] a nonlinear model that relies on a 2nd-order polynomial expansion of the nonlinearity,

$$\boldsymbol{\mu}(\mathbf{M}, \mathbf{a}_p, \mathbf{b}_p) \triangleq b_p (\mathbf{M} \mathbf{a}_p) \odot (\mathbf{M} \mathbf{a}_p) \quad (9)$$

leading to the following polynomial post-nonlinear mixing model (PPNM)

$$\mathbf{y}_p^{(\text{PPNM})} = \mathbf{M} \mathbf{a}_p + b_p (\mathbf{M} \mathbf{a}_p) \odot (\mathbf{M} \mathbf{a}_p) + \mathbf{n}_p. \quad (10)$$

The PPNM has demonstrated a noticeable flexibility to model various nonlinearities not only for unmixing purposes [16] but also to detect nonlinear mixtures in the observed image [25]. This model has also the great advantage of having the amount of nonlinearity to be governed by a unique parameter b_p in each pixel, contrary to NM or GBM. Straightforward computations also show that PPNM includes bilinear terms $\mathbf{m}_i \odot \mathbf{m}_j$ ($j \neq i$) similar to those involved in the NM, FM and GBM, and also quadratic terms $\mathbf{m}_i \odot \mathbf{m}_i$, which may account for interactions between similar materials.

C. Unmixing algorithms

To evaluate the accuracy of the mixing models of interest, the pixels of the in-situ and simulated data are unmixed with respect to each model. When analyzing the pixels with the LMM, the nonlinear contribution $\mu(\mathbf{M}, \mathbf{a}_p, \mathbf{b}_p)$ is set to zero. Based on the prior knowledge of the endmember signatures \mathbf{M} , the abundance vector \mathbf{a}_p associated with each pixel \mathbf{y}_p is estimated by solving the constrained minimization problem

$$\hat{\mathbf{a}}_p = \underset{\mathbf{a}_p}{\operatorname{argmin}} \|\mathbf{y}_p - \mathbf{M}\mathbf{a}_p\|_2^2 \quad \text{s.t.} \quad (2). \quad (11)$$

In this work, to solve this problem, the fully constrained least square (FCLS) algorithm [4] is used.

Moreover, when analyzing the pixels with nonlinear mixing models, the abundance vector \mathbf{a}_p and the nonlinearity parameter vector \mathbf{b}_p associated with each pixel \mathbf{y}_p are estimated by solving the following constrained optimization problem

$$(\hat{\mathbf{a}}_p, \hat{\mathbf{b}}_p) = \underset{\mathbf{a}_p, \mathbf{b}_p}{\operatorname{argmin}} \|\mathbf{y}_p - \mathbf{M}\mathbf{a}_p - \mu(\mathbf{M}, \mathbf{a}_p, \mathbf{b}_p)\|_2^2. \quad (12)$$

Depending on the considered model, the set of constraints imposed to the abundance vector \mathbf{a}_p and the possible nonlinear coefficient vector \mathbf{b}_p may differ. For the FM, GBM and PPNM, the abundance vector \mathbf{a}_p should satisfy the LMM-based constraints (2), while for the NM, this constraint is applied to the joint vector $[\mathbf{a}_p, \mathbf{b}_p]$. Similarly, the nonlinear coefficient vector \mathbf{b}_p for the GBM and PPNM should satisfy constraints that depend on the considered model and the nonlinearity component $\mu(\mathbf{M}, \mathbf{a}_p, \mathbf{b}_p)$ in (4) or (9) depends also on the considered nonlinear model.

For the experimental results reported in Section IV, the FCLS algorithm is used to solve the NM-based unmixing problem since NM can be interpreted as a linear mixture of an extended set of endmembers, as shown in [21]. The FM parameters are estimated with the algorithm detailed in [22], based on a first-order Taylor series expansion of the nonlinearity $\mu(\mathbf{M}, \mathbf{a}_p, \mathbf{b}_p)$. Finally, The gradient descent and the subgradient descent algorithms developed in [26] and [16] are used to solve the GBM- and PPNM-based unmixing problems, respectively. Interested readers are invited to refer to these works for detailed information regarding the optimization schemes.

III. DATA DESCRIPTION

The mixing models and corresponding unmixing algorithms detailed in the previous sections are compared using simulated and real hyperspectral images. It is worth noting that, for both kinds of datasets, actual pure component spectral signatures (i.e., endmember spectra) and quantitative spatial distributions of these components (i.e., abundances) are available as ground truth in each pixel of the considered images. These datasets¹ are described in this section.

¹These datasets will be available online. Please contact the authors.

A. Simulated dataset

Two types of synthetic hyperspectral image data were generated from a ray tracing experiment. First, synthetic but realistic fully calibrated virtual scenes, namely citrus orchards and a forest, have been designed using methods developed in [18] and [27], respectively. Then, corresponding hyperspectral images have been simulated using an extended version of the physically based ray tracer (PBRT) [28]. In PBRT, a scene is defined using submodels to describe the various components of the scene: illumination sources, sensor platform, material optical properties, integrator and geometry descriptions. For the different generated images, the illumination has been modelled to closely agree with the average circadian illumination from April until September, corresponding to a midlatitude northern hemisphere growing season. The illumination has been composed of a combination of direct and diffuse light calculated from 350 to 2500nm with a 10nm interval. The citrus trees and weeds of the orchard scenes (see paragraph III-A1) and the trees of the forest scene (see paragraph III-A2) have been constructed as triangular meshes by implementing the algorithm introduced in [29]. Their material properties have been described by a bidirectional scattering distribution function (BSDF) model [18].

1) *Orchard scenes*: The fully calibrated virtual citrus orchard developed in [18] has been used to create two different orchard scenes: (i) an orchard consisting of citrus trees and a soil background, leading to two-endmember mixtures and (ii) an orchard consisting of citrus trees, a soil background and weed patches, leading to three-endmember mixtures. Each orchard scene consists of 20×20 pixels, with a pixel size of $2\text{m} \times 2\text{m}$. The reference spectral signatures are known for the three components, as well as the exact per-pixel abundances.

The orchards have been constructed with a row spacing of 4.5m, tree spacing of 2m, row azimuth of 7.3° and an average tree height of 3m. This composition is consistent with the reference orchard, located in Wellington, South Africa (33.58°S , 18.93°E), used to calibrate the virtual orchard [18]. Spectral input data for citrus leaves and stems, soils and weeds have been measured using a full-range (350-2500nm) analytic spectral devices (ASD) Fieldspec JR spectroradiometer with a 25° foreoptic. The weed spectrum has been chosen as of the *Lolium* sp. species. A Haplic Arenosol [30] typical for commercial citrus orchards in the Western Cape Province in South Africa has been used in the simulations [31]. An example of a high resolution image of $20\text{m} \times 20\text{m}$ of the two-endmember orchard is depicted in Fig 1 (a), while the three-endmember orchard is shown in Fig 1 (b). For a detailed description of the design, modalities and application of the virtual orchard, the reader is invited to consult [18].

2) *Forest scene*: To simulate the forest scene, 3D tree geometry descriptions were available for *Fagus sylvatica* L. and *Populus nigra* L. var. "*italica*" Muench. Each tree was characterized by

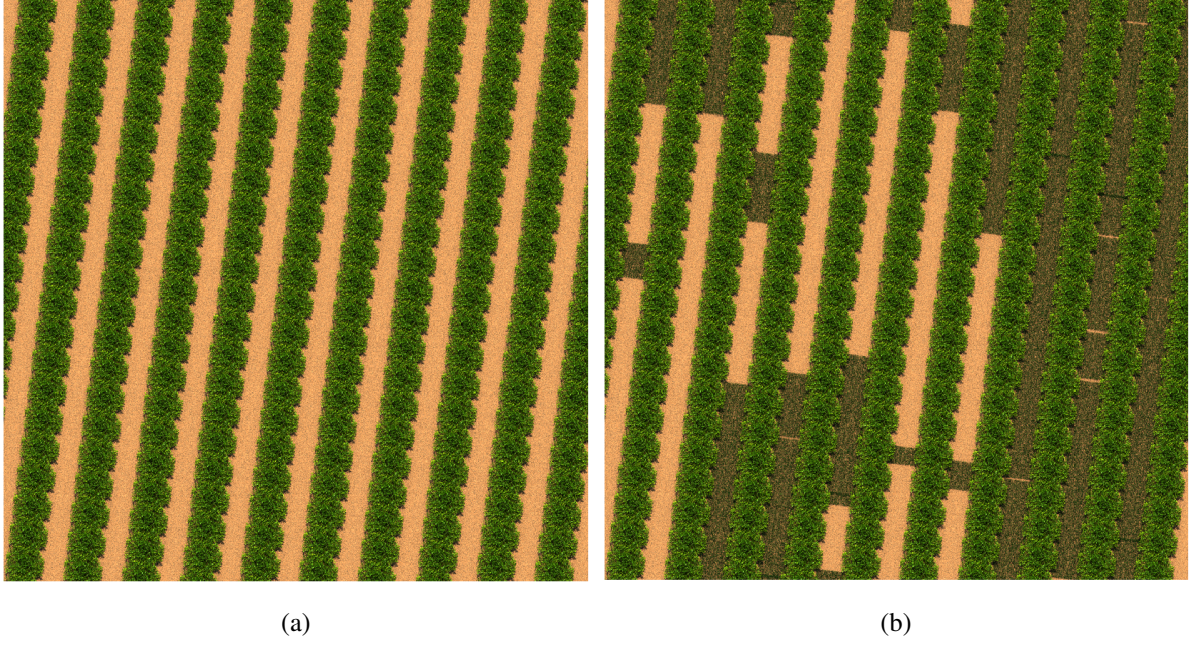


Fig. 1: High resolution images of the two orchards with (a) two endmembers, i.e., tree and soil, and (b) three endmembers, i.e., tree, soil and weeds.

a specific structure based on its age (i.e., 20 years old). All leaves were assigned a species-specific reflectance and transmittance spectrum extracted from the leaf optical properties experiment (LOPEX) dataset [32].

The virtual forest consisted of trees selected from the species-specific tree pools as described above. To achieve a nearly 100% canopy cover, the average tree spacing has been set to 5m for the beech trees and 1m for the poplars. A series of six forest scenes has been rendered providing a gradual transition from a forest scene completely dominated by one species to a scene dominated by the other species. More precisely, 20% of the beech trees have been randomly replaced by poplar trees in the subsequent scene. Each forest scene consisted of 15×15 pixels, with a pixel size of $30\text{m} \times 30\text{m}$. In Fig 2, a detail is shown of a 30m pixel, for the forest consisting of 60% beech trees and 40% poplars. Note here that the spatial resolution of the forest scene is significantly larger than the resolution of the orchard scene detailed in paragraph III-A1. These choices allow different plant production systems to be covered, with various species combinations, sets of endmembers and spatial resolution scales.

B. In-situ measurement

In addition, an experiment was conducted in the same orchard used for the calibration of the virtual orchard described in paragraph III-A1. The inter-row spacing of the 3m tall trees was 4.5m and the inter-tree spacing 2.5m. The row azimuth was 7.3° . The soil had a sandy texture and an organic

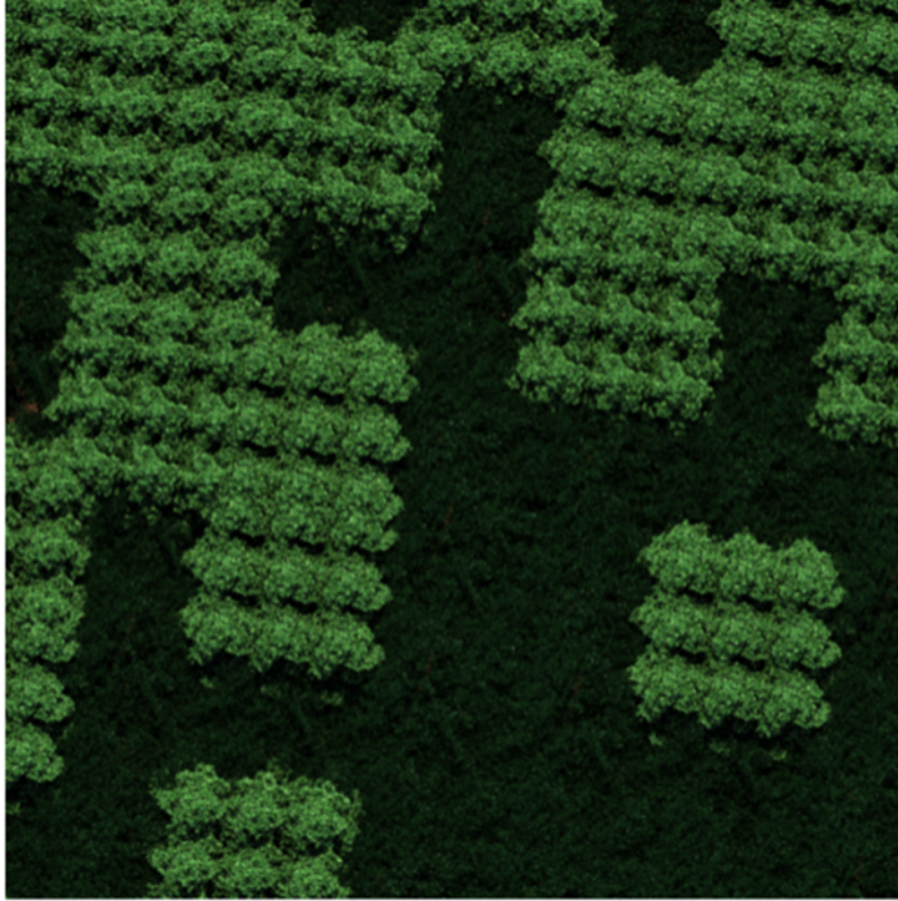


Fig. 2: High resolution detail of a 30m pixel of the forest with 60% beech trees and 40% poplars.

carbon concentration of 0.53%. Significant weed cover, dominantly *Lolium* sp. L. ($\approx 30\%$ of the inter-row spacing, concentrated in dense patches) was present.

Throughout the orchard, in-situ measured reflectance spectra of 60 mixed ground plots were collected, i.e., 25 mixtures of tree and soil, 25 mixtures of tree and weed, and 25 mixtures of tree, soil and weed. Reflectance measurements were performed in August using a spectroradiometer with a 25° fore-optic, covering the 350 – 2500nm spectral domain (Analytic Spectral Devices, Boulder, USA). The measurements were taken from nadir at a height of 4m. For each measured mixed pixel, the plot-specific pure endmember spectra and ground cover fraction distributions were determined. The plot-specific endmembers were acquired by measuring a number of pure soil and sunlit crown spectra in each plot, as illustrated in Fig. 3. Information on the ground cover composition of each of the measured mixed pixels was extracted from digital photographs (SONY DSC-P8/3.2 megapixel cyber shot camera, positioned in nadir). A more detailed description on the experimental setup, depicted in Fig. 3, can be found in [12].



Fig. 3: Experimental set-up to determine a plot-specific soil and sunlit crown endmember for each plot. Plot-specific endmembers were used in the spectral mixture analysis to isolate the impact of nonlinear mixing from endmember variability (from [12]).

IV. EXPERIMENTAL RESULTS

The relevance of the mixing models under test, namely LMM, FM, NM, GBM and PPNM, and associated unmixing algorithms, is evaluated with respect to i) their ability of accurately describing the physical processes yielding the considered mixtures and ii) their ability of providing meaningful estimations of the abundance coefficients, to properly account for the spatial distribution of the materials over each observed pixel. More precisely, let $\hat{\mathbf{a}}_p$ and $\hat{\mathbf{b}}_p$ denote the abundance and nonlinearity coefficient vectors estimated by the algorithms introduced in paragraph II-C. First, the average square reconstruction error (RE) is measured as

$$\text{RE} = \frac{1}{LP} \sum_{p=1}^P \|\mathbf{y}_p - \hat{\mathbf{y}}_p\|^2 \quad (13)$$

where $\|\cdot\|$ stands for the usual Euclidean norm ($\|\mathbf{x}\| = \sqrt{\mathbf{x}^T \mathbf{x}}$). In the right-hand side of (13), \mathbf{y}_p ($p = 1, \dots, P$) are the observed pixels whereas $\hat{\mathbf{y}}_p$ are the corresponding estimates given by

$$\hat{\mathbf{y}}_p = \mathbf{M}\hat{\mathbf{a}}_p + \boldsymbol{\mu}(\mathbf{M}, \hat{\mathbf{a}}_p, \hat{\mathbf{b}}_p) \quad (14)$$

where $\boldsymbol{\mu}(\cdot)$ is equal to 0 for the LMM or stands for the additional nonlinear contribution for the nonlinear models (see Section II).

Since the actual endmember spectra and abundance coefficients (that satisfy the constraints in (2)) are perfectly known for each pixel of the considered scenes, these REs can also be computed from

pixels reconstructed following the LMM and FM with the actual values of the abundances. These two “oracle” models are denoted o-LMM and o-FM in what follows. In particular, the RE associated with the o-LMM provides interesting information regarding the actual level of nonlinearities in the considered pixels. Note also that such oracle performance can not be computed for the other nonlinear models, since NM is based on a different abundance definition (e.g., they do not follow the constraints (2)) and GBM and PPNM require the prior knowledge of additional (unknown) parameters.

Moreover, to visualize the reconstruction error as a function of the wavelength, a signed error, defined as the mean reconstruction difference in the ℓ th band, is also computed as

$$\text{RD}_\ell = \frac{1}{P} \sum_{p=1}^P (y_{\ell,p} - \hat{y}_{\ell,p}). \quad (15)$$

Finally, to measure the accuracy of the abundance estimation, the mean square errors (MSE) between the actual abundance vectors \mathbf{a}_p and the corresponding estimated $\hat{\mathbf{a}}_p$ ($p = 1, \dots, P$) are computed as follows

$$\text{MSE} = \frac{1}{RP} \sum_{p=1}^P \|\mathbf{a}_p - \hat{\mathbf{a}}_p\|^2. \quad (16)$$

A. Simulated dataset

1) *Virtual orchard*: The unmixing results for the simulated orchard scenes are shown in Table I in terms of MSE and RE. From these results, for both two- and three-endmembers, one can conclude that NM and LMM perform similarly in term of RE, while PPNM and FM provide the best results and, in particular, significantly better than LMM. Regarding the abundance MSE, NM and LMM provide similar errors for two-endmember mixtures and all nonlinear models perform better than LMM for three-endmember mixtures.

In Fig. 4, the RDs are depicted as functions of wavelength, for the different linear and nonlinear mixing models. From this figure, it appears that the nonlinearities occurring in spectral bands ranging from 1400nm to 2500nm are of high intensity (see the plot associated with the oracle-LMM, in black dashed line) but are rather well described by the various nonlinear models.

2) *Virtual forest*: For the simulated forest scenes, the unmixing results are reported in Table II. These results are computed for four scene compositions, with increasing proportions from 20% to 80% of beech trees with respect to poplars (see paragraph III-A2). The first three images provided a sequence of images with increasing nonlinearity, as shown by the RE obtained with the oracle-LMM, ranging from 0.71 to 1.67 ($\times 10^{-4}$). The fourth image, composed of 80% of poplars and 20% of beech trees, seems to be subject to nonlinearities of lower intensity, since the oracle-LMM RE is 0.68×10^{-4} .

As with the previous dataset, PPNM together with NM provides the best model fit for all images, i.e. with lowest RE, and the best abundance estimates in terms of MSE. The abundance estimation

		2 endm.	3 endm.
RE	LMM	7.70	5.81
	o-LMM	15.0	10.40
	FM	1.24	0.91
	o-FM	10.20	7.66
	NM	7.70	5.81
	GBM	10.13	0.94
	PPNM	1.28	0.91
MSE	LMM	0.96	3.17
	FM	1.13	2.27
	NM	0.92	2.44
	GBM	1.47	2.45
	PPNM	1.22	2.62

TABLE I: Two- and three-endmember orchard synthetic dataset. Abundance MSE ($\times 10^{-2}$) and RE ($\times 10^{-4}$) for various linear/nonlinear mixing models.

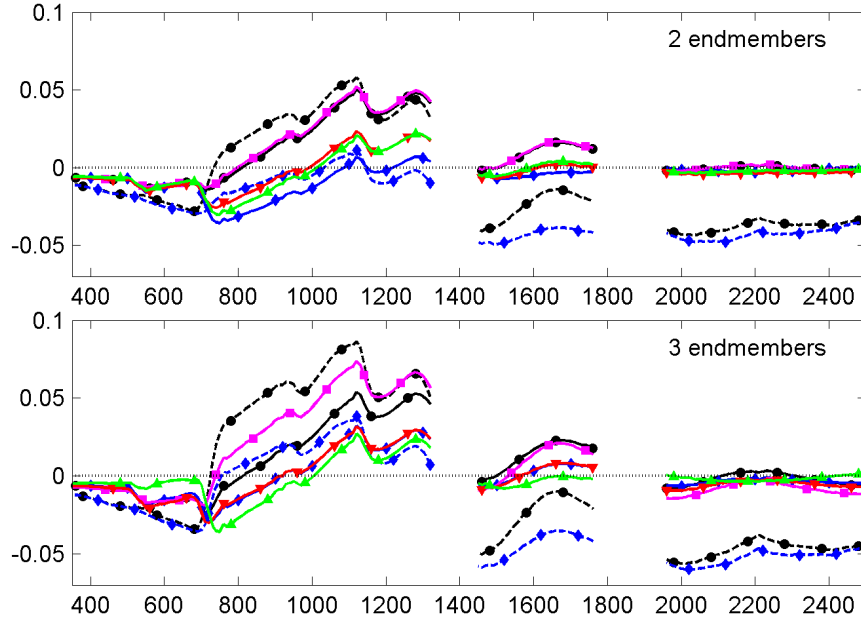


Fig. 4: Two- and three-endmember orchard synthetic dataset. Reconstruction difference RD_ℓ as a function of wavelength for various linear/nonlinear mixing models: LMM (black), oracle-LMM (black, dashed line), FM (blue), oracle-FM (blue, dashed line), NM (magenta), GBM (red) and PPNM (green).

performance of the different models is also decreasing with increasing nonlinear mixing effects in the images, even though the RE remained almost constant for NM and PPNM. FM performed poorly

and LMM and GBM lead to similar results.

%beech		0.2	0.4	0.6	0.8
%pop		0.8	0.6	0.4	0.2
RE	LMM	0.95	1.92	2.06	0.99
	o-LMM	0.71	1.37	1.67	0.68
	FM	4.45	8.23	10.7	13.0
	o-FM	2.60	11.06	20.0	13.6
	NM	0.30	0.32	0.31	0.16
	GBM	0.94	1.92	2.06	0.99
	PPNM	0.13	0.15	0.14	0.12
MSE	LMM	1.07	3.47	6.75	4.23
	FM	5.62	6.83	9.50	7.73
	NM	0.40	1.07	1.33	0.75
	GBM	1.07	3.49	6.79	4.27
	PPNM	0.57	1.15	1.35	0.88

TABLE II: Two-endmember forest synthetic dataset. Abundance MSE ($\times 10^{-2}$) and RE ($\times 10^{-4}$) for various linear/nonlinear mixing models.

Fig. 5 shows the RDs as functions of wavelength. From the RD associated with the oracle-LMM, it clearly appears that the nonlinearity effects mostly occur in the spectral range 700nm – 1400nm, especially for the 20 – 80% and 80 – 20% scenes. All nonlinear mixing models provide good model fits, except the FM, as already shown by the REs reported in Table II.

B. In-situ measurements

Three types of in-situ measured mixed pixels were available to test the different mixing models, i.e., tree-weed, tree-soil and tree-soil-weed mixtures (see paragraph III-B). In Table III, the reconstruction error of the mixed signal and the accuracy of the estimated abundances are depicted. From the RE associated with the oracle-LMM, it appears that most nonlinearities occur in the tree-soil mixtures. Once again, PPNM is the mixing model that reconstructs the mixed signatures the best, while FM performed worse than the LMM. For the abundance accuracy, MSE results are less homogeneous than those obtained with the various simulated datasets. Depending on the type of the mixture, GBM or PPNM are the best unmixing model, while FM gives the lowest abundance estimation accuracies.

The RDs obtained on the in-situ measurements are depicted in Fig. 6. Similarly to the previous analyzed dataset, most of the nonlinear effects seem to occur in the 700nm – 1400nm spectral range,

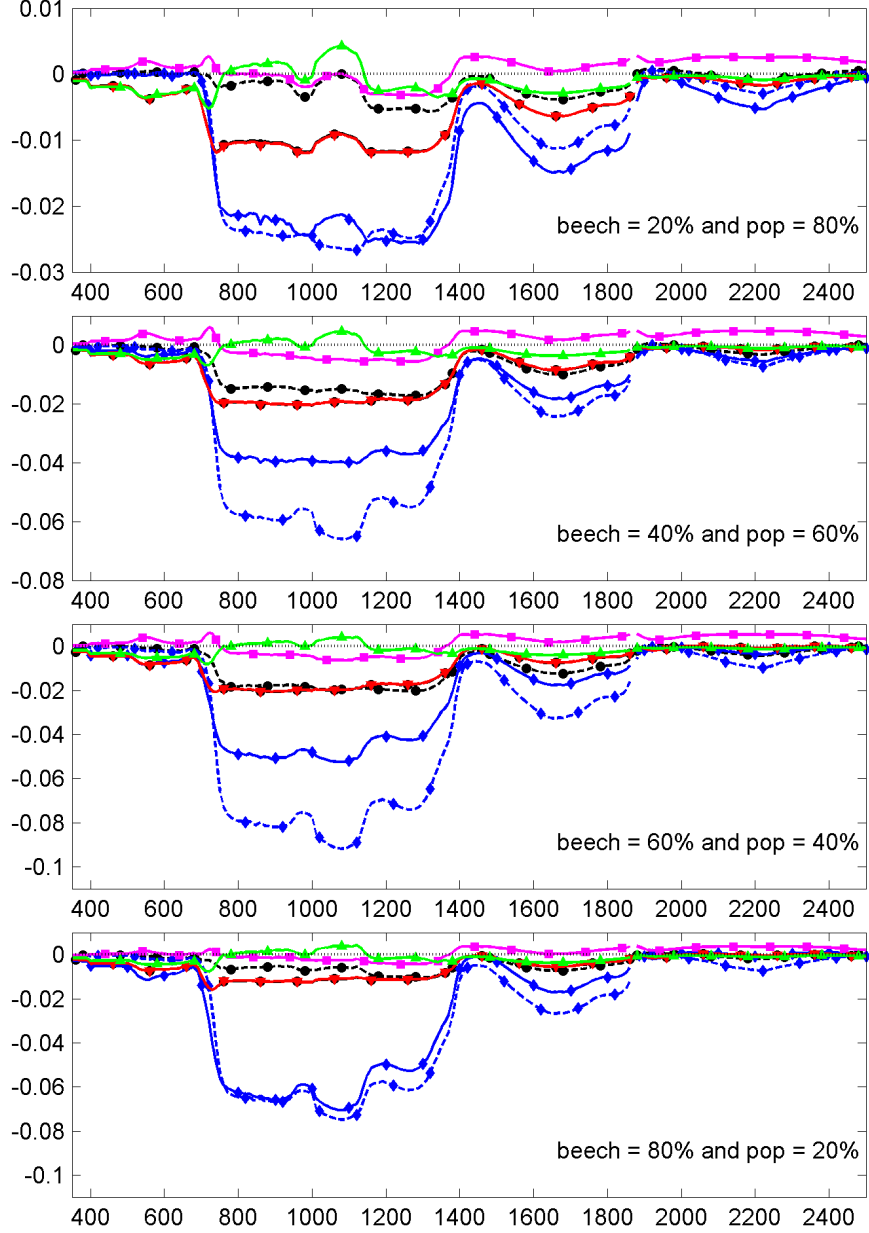


Fig. 5: Two-endmember forest synthetic dataset. Reconstruction difference RD_ℓ as a function of wavelength for various linear/nonlinear mixing models: LMM (black), oracle-LMM (black, dashed line), FM (blue), oracle-FM (blue, dashed line), NM (magenta), GBM (red) and PPNM (green).

while being very small in the visible range. From these plots, most of the mixing model appear not sufficiently accurate to capture the nonlinearities in the observed mixtures, except the PPNM.

V. DISCUSSION

The various datasets used during the experiments enable the assessment of the performance of different unmixing models, and the evaluation of the relevance of using nonlinear mixing models

		tree-weed	tree-soil	tree-soil-weed
RE	LMM	16.4	27.1	6.80
	o-LMM	33.9	50.0	37.4
	FM	17.7	16.4	10.9
	o-FM	26.0	40.7	53.0
	NM	16.3	26.8	2.13
	GBM	15.9	15.2	6.71
	PPNM	3.07	1.82	1.21
MSE	LMM	12.5	2.78	6.42
	FM	13.5	2.88	8.15
	NM	12.6	2.71	5.80
	GBM	12.2	2.86	6.39
	PPNM	13.0	2.57	4.83

TABLE III: Two- and three-endmember in-situ measurements. Abundance MSE ($\times 10^{-2}$) and RE ($\times 10^{-4}$) for various linear/nonlinear mixing models.

to properly describe mixtures observed in vegetated areas. As the exact per-pixel endmembers are known, the effects of endmember spectral variability can be strongly reduced. Consequently, the simulated or measured mixed pixels can be fully characterized by the abundances, and the influence of the nonlinear mixing effects on the unmixing accuracy could be evaluated. To qualitatively and quantitatively evaluate the mixing models and corresponding unmixing algorithms, general trends emerge from the results presented in Section IV. These findings are reported in what follows.

A. Quantifying the amount of nonlinearity

Since the endmember signatures as well as the abundance coefficients are perfectly known for each pixel of the considered scenes, the modeling error (i.e., the RE) obtained with the oracle-LMM could be considered as the mis-modeling introduced by nonlinear mixing effects. For all three data sets, a significant RE can be observed with the oracle-LMM, demonstrating the presence of nonlinear mixing effects, as already shown in [11], [12], [33], for examples. Overall, from the results reported in the previous section, the mixed pixel signatures seem to be better represented by nonlinear mixing models, and specifically PPNM. However, all nonlinear mixing models can not be advocated to better describe mixed pixels than LMM, such as the GBM and NM for the simulated orchard data (see Table I), and the FM for the simulated forest data (see Table II) and the in-situ orchard data (see Table III). This shows that these nonlinear mixing models do not necessarily better represent the

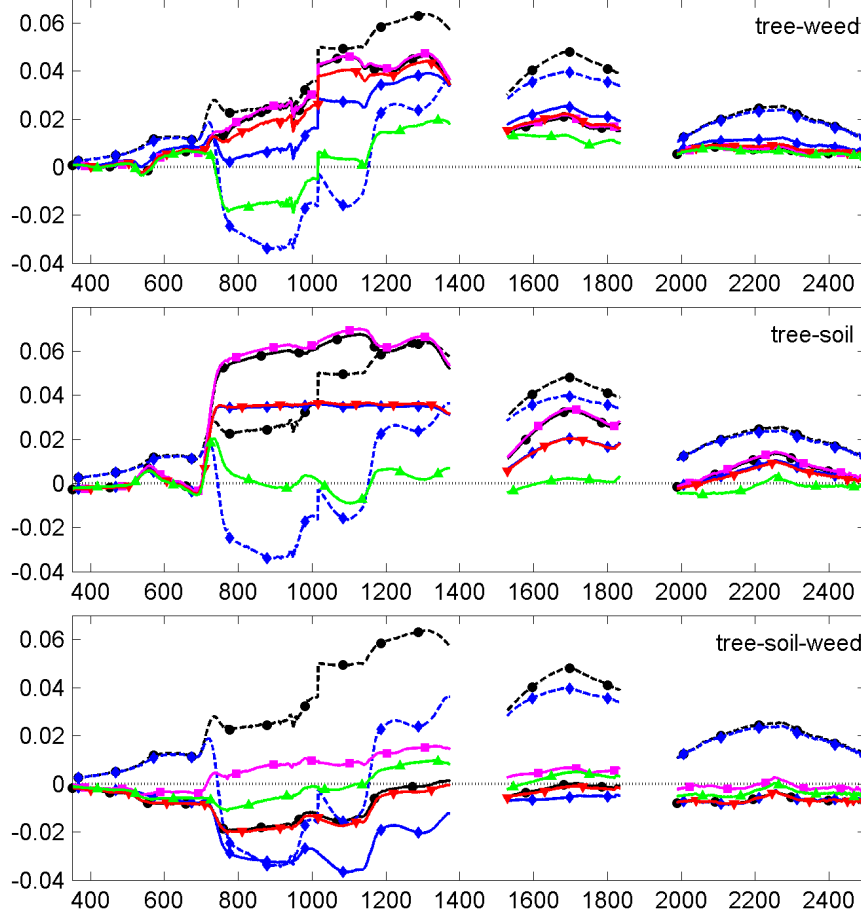


Fig. 6: Two- and three-endmember in-situ measurements. Reconstruction difference RD_ℓ as a function of wavelength for various linear/nonlinear mixing models: LMM (black), oracle LMM (black, dashed line), FM (blue), oracle FM (blue, dashed line), NM (magenta), GBM (red) and PPNM (green).

mixed signatures.

B. On the use of reconstruction error to assess a mixing model

It is also important to note that a better modeling of the mixed pixels does not necessarily result in a better estimation of the abundances. For instance, PPNM, which has been shown to be the most accurate to model nonlinearly mixed spectral signatures, sometimes lead to less accuracy with respect to the abundance estimation when compared to LMM, in particular for the two-endmember mixtures in the simulated orchard data (see Table I) and for the tree-weed mixtures in the in-situ data (see Table III). In the results of the simulated forest, the same trend can be observed: in spite of increasing nonlinear mixing effects, the REs remain almost constant for both the PPNM and the NM, while the accuracy of the estimated abundances decreases (see Table II). As a consequence, the model fitting error, widely used in the remote sensing literature to monitor the performance of the unmixing

algorithm, can not be used as the unique figure-of-merit to evaluate the relevance of a given mixing model.

C. Mis-modeling with respect to wavelength

All nonlinear mixing models considered in Section II and used in the experiments reported in Section IV implicitly assume the same amount of nonlinearity for each wavelength of the spectral domain. Indeed, they are basically defined by cross-products between the endmember spectra, without introducing any weighting functions that would depend on the spectral bands. However, from the RDs depicted in Fig.'s 4, 5 and 6, it clearly appears that the mis-modeling is drastically subjected to the influence of the wavelength. This corroborates the results of Somers *et al.* who also noticed similar behavior for the bilinear mixing model [13]. Most of the nonlinear models under test lead to reconstructed mixtures with the same admissible accuracy as the LMM in the visible range (400nm – 700nm). Conversely, a clear degradation of the modeling performance can be observed in the 700nm – 1400nm spectral range for most linear and nonlinear models, except for the PPNM. In particular, the RDs associated with the oracle-LMM demonstrate the important level of nonlinearity in the near-infrared region.

D. Dealing with the unmixing algorithm intrinsic limitations

For both LMM and FM models, oracle measures of performance have been computed since these models are fully described by the a priori known abundance coefficients, explicitly considered as the spatial distributions of the materials over the imaged pixels. However, for the other nonlinear mixing models, unmixing algorithms need to be used to infer all the parameters involved in the model specification (e.g., abundances and nonlinearity parameters). Unfortunately, the optimization problems to be solved, formulated in (11) and (12), to recover the abundance coefficients are not totally straightforward, mainly due to the constraints and/or the nonlinearity. As a consequence, the reliability of the obtained results, in terms of RE and abundance MSE, should be carefully analyzed, indeed mitigated. More precisely, part of the REs may consist of approximation errors induced by the unmixing algorithms themselves, in particular when these iterative algorithms converge toward a stationary point which is not the global minimizer of the objective function. Consequently, the abundance estimates may be biased since subjected to these approximation errors. As a manifest example, when considering the forest synthetic dataset, REs associated with the oracle-LMM are always lower than the REs obtained with the LMM-based unmixing algorithm (see Table II). This is an archetypal instance of the limitations of the LMM-based unmixing algorithm.

VI. CONCLUSION

This paper attempted to make a first step toward a full quantitative assessment of linear and nonlinear mixing models to properly described mixtures observed in hyperspectral images acquired over vegetated areas. The conducted work exploited two kinds of hyperspectral data, whose main advantages lies in the availability of ground truth, that consists of the actual material signatures (endmember spectra) and their corresponding spatial repartitions in the pixels (abundance coefficients). The first set of hyperspectral data consisted of physically-based simulated images, while the second set of hyperspectral data came from real in-situ measurements. Various linear and nonlinear mixing models were used to analyze these data. They were evaluated in terms of spectral mis-modeling (i.e., reconstruction error) and abundance estimation accuracy. From the obtained results, it clearly appeared that the polynomial post-nonlinear mixing model undeniably provided, by far, the best reconstruction of the mixed pixels. It also persistently led to admissible abundance estimates, regardless of the considered scene. More generally, depending of the analyzed mixtures, the Nascimento model, the Fan model or the polynomial post-nonlinear model provided the most interesting results with respect to the abundance estimates. However, it was worth noting that the results presented in this work needed to be mitigated by the intrinsic limitations of the resorted unmixing algorithms, that could induced estimate biases.

REFERENCES

- [1] J. M. Bioucas-Dias, A. Plaza, N. Dobigeon, M. Parente, Q. Du, P. Gader, and J. Chanussot, "Hyperspectral unmixing overview: Geometrical, statistical, and sparse regression-based approaches," *IEEE J. Sel. Topics Appl. Earth Observations and Remote Sens.*, vol. 5, no. 2, pp. 354–379, April 2012.
- [2] N. Keshava and J. F. Mustard, "Spectral unmixing," *IEEE Signal Process. Mag.*, vol. 19, no. 1, pp. 44–57, Jan. 2002.
- [3] B. Somers, G. P. Asner, and L. Tits, "Endmember variability in spectral: a review," *Remote Sens. Environment*, vol. 115, no. 7, pp. 1603–1616, July 2011.
- [4] D. C. Heinz and C. -I Chang, "Fully constrained least-squares linear spectral mixture analysis method for material quantification in hyperspectral imagery," *IEEE Trans. Geosci. and Remote Sensing*, vol. 29, no. 3, pp. 529–545, March 2001.
- [5] C. Theys, N. Dobigeon, J.-Y. Tournet, and H. Lantéri, "Linear unmixing of hyperspectral images using a scaled gradient method," in *Proc. IEEE-SP Workshop Stat. and Signal Processing (SSP)*, Cardiff, UK, Aug. 2009, pp. 729–732.
- [6] R. Heylen, D. Burazerovic, and P. Scheunders, "Fully constrained least squares spectral unmixing by simplex projection," *IEEE Trans. Geosci. and Remote Sensing*, vol. 49, no. 11, pp. 4112–4122., Nov. 2011.
- [7] N. Dobigeon, J.-Y. Tournet, and C.-I Chang, "Semi-supervised linear spectral unmixing using a hierarchical Bayesian model for hyperspectral imagery," *IEEE Trans. Signal Process.*, vol. 56, no. 7, pp. 2684–2695, July 2008.
- [8] O. Echès, N. Dobigeon, C. Mailhes, and J.-Y. Tournet, "Bayesian estimation of linear mixtures using the normal compositional model. Application to hyperspectral imagery," *IEEE Trans. Image Process.*, vol. 19, no. 6, pp. 1403–1413, June 2010.

- [9] O. Eches, N. Dobigeon, J.-Y. Tourneret, and H. Snoussi, "Variational methods for spectral unmixing of hyperspectral unmixing," in *Proc. IEEE Int. Conf. Acoust., Speech, and Signal Processing (ICASSP)*, Prague, Czech Republic, May 2011, pp. 957–960.
- [10] N. Dobigeon, J.-Y. Tourneret, C. Richard, J. C. M. Bermudez, S. McLaughlin, and A. O. Hero, "Nonlinear unmixing of hyperspectral images: Models and algorithms," *IEEE Signal Process. Mag.*, vol. 31, no. 1, pp. 89–94, Jan. 2014.
- [11] L. Tits, W. Delabastita, B. Somers, J. Farifteh, and P. Coppin, "First results of quantifying nonlinear mixing effects in heterogeneous forests: A modeling approach," in *Proc. IEEE Int. Conf. Geosci. Remote Sens. (IGARSS)*, 2012, pp. 7185–7188.
- [12] B. Somers, K. Cools, S. Delalieux, J. Stuckens, D. V. der Zande, W. W. Verstraeten, and P. Coppin, "Nonlinear hyperspectral mixture analysis for tree cover estimates in orchards," *Remote Sens. Environment*, vol. 113, pp. 1183–1193, Feb. 2009.
- [13] B. Somers, L. Tits, and P. Coppin, "Quantifying nonlinear spectral mixing in vegetated areas: computer simulation model validation and first results," *IEEE J. Sel. Topics Appl. Earth Observations and Remote Sens.*, 2014, to appear.
- [14] Y. Altmann, N. Dobigeon, and J.-Y. Tourneret, "Bilinear models for nonlinear unmixing of hyperspectral images," in *Proc. IEEE GRSS Workshop Hyperspectral Image Signal Process.: Evolution in Remote Sens. (WHISPERS)*, Lisbon, Portugal, June 2011, pp. 1–4.
- [15] I. Meganem, P. Déliot, X. Briottet, Y. Deville, and S. Hosseini, "Linear-quadratic mixing model for reflectances in urban environments," *IEEE Trans. Geosci. and Remote Sensing*, vol. 52, no. 1, pp. 544–558, Jan. 2014.
- [16] Y. Altmann, A. Halimi, N. Dobigeon, and J.-Y. Tourneret, "Supervised nonlinear spectral unmixing using a post-nonlinear mixing model for hyperspectral imagery," *IEEE Trans. Image Process.*, vol. 21, no. 6, pp. 3017–3025, June 2012.
- [17] O. Eches and M. Guillaume, "A bilinear-bilinear non-negative matrix factorization method for hyperspectral unmixing," *IEEE Geosci. and Remote Sensing Lett.*, vol. 11, no. 4, pp. 778–782, April 2014.
- [18] J. Stuckens, B. Somers, S. Delalieux, W. W. W. Verstraeten, and P. Coppin, "The impact of common assumptions on canopy radiative transfer simulations: a case study in citrus orchards," *J. Quantitative Spectroscopy and Radiative Transfer*, vol. 110, no. 1–2, pp. 1–21, Jan. 2009.
- [19] D. V. der Zande, J. S. W. W. Verstraeten, B. Muys, and P. Coppin, "Assessment of light dynamics in broadleaved forest canopies using terrestrial laser scanning," *Remote Sensing*, vol. 2, no. 6, pp. 1564–1474, 2010.
- [20] L. Tits, W. D. Keersmaecker, B. Somers, G. P. Asner, J. Farifteh, and P. Coppin, "Hyperspectral shape-based unmixing to improve intra- and interclass variability for forest and agro-ecosystem monitoring," *ISPRS J. Photogrammetry and Remote Sensing*, vol. 74, pp. 163–174, Nov. 2012.
- [21] J. M. P. Nascimento and J. M. Bioucas-Dias, "Nonlinear mixture model for hyperspectral unmixing," in *Proc. SPIE Image and Signal Processing for Remote Sensing XV*, L. Bruzzone, C. Notarnicola, and F. Posa, Eds., vol. 7477, no. 1. SPIE, 2009, p. 74770I.
- [22] W. Fan, B. Hu, J. Miller, and M. Li, "Comparative study between a new nonlinear model and common linear model for analysing laboratory simulated-forest hyperspectral data," *Int. J. Remote Sens.*, vol. 30, no. 11, pp. 2951–2962, June 2009.
- [23] A. Halimi, Y. Altmann, N. Dobigeon, and J.-Y. Tourneret, "Nonlinear unmixing of hyperspectral images using a generalized bilinear model," *IEEE Trans. Geosci. and Remote Sensing*, vol. 49, no. 11, pp. 4153–4162, Nov. 2011.
- [24] A. Taleb and C. Jutten, "Source separation in post-nonlinear mixtures," *IEEE Trans. Signal Process.*, vol. 47, no. 10, pp. 2807–2820, Oct. 1999.
- [25] Y. Altmann, N. Dobigeon, and J.-Y. Tourneret, "Nonlinearity detection in hyperspectral images using a polynomial post-nonlinear mixing model," *IEEE Trans. Image Process.*, vol. 22, no. 4, pp. 1267–1276, April 2013.
- [26] A. Halimi, Y. Altmann, N. Dobigeon, and J.-Y. Tourneret, "Unmixing hyperspectral images using the generalized

- bilinear model,” in *Proc. IEEE Int. Conf. Geosci. Remote Sens. (IGARSS)*, Vancouver, Canada, July 2011, pp. 1886–1889.
- [27] D. Van der Zande, “Mathematical Modeling of 3D Canopy Structure in Forest Stands Using Ground-Based Lidar,” Ph.D. dissertation, Katholieke Universiteit Leuven, Leuven, Belgium, 2008.
- [28] M. Pharr and G. Humphreys, *Physically Based Rendering: From Theory to Implementation*, T. Cox, Ed. San Francisco: Morgan Kaufmann Pub, 2004.
- [29] J. Weber and J. Penn, “Creation and rendering of realistic trees,” in *Proc. SIGGRAPH Annu. Conf. Comput. Graph. Interactive Techn.*, 1995, pp. 119–128.
- [30] FAO, “FAO world reference base for soil resources,” Food and Agriculture Organisation of the United Nations, Rome, World Soil Resource Report 84, 1998.
- [31] B. Somers, V. Gysels, W. Verstraeten, S. Delalieux, and P. Coppin, “Modelling moisture-induced soil reflectance changes in cultivated sandy soils: a case study in citrus orchards,” *European J. Soil Sci.*, vol. 61, no. 6, pp. 1091–1105, 2010.
- [32] B. Hosgood, S. Jacquemoud, G. Andreoli, J. Verdebout, A. Pedrini, and G. Schmuck, “Leaf Optical Properties EXperiment 93 (LOPEX93),” Joint Research Centre / Institute for Remote Sensing Applications Unit for Advanced Techniques, Ispra, Italy, Report EUR 16095 EN, 1995.
- [33] C. C. Borel and S. A. W. Gerstl, “Nonlinear spectral mixing model for vegetative and soil surfaces,” *Remote Sens. Environment*, vol. 47, no. 3, pp. 403–416, 1994.